Lecture 13 (09.12.2020)

Dissipation and Quality Factor

I. Dissipation

Mechanical dissipation (or the friction coefficient) quantifies the energy loss to the environment by an oscillator. Recall our harmonic oscillator equation of motion:

$$m\ddot{x} + \Gamma\dot{x} + kx = F(t) \qquad k = m\omega_0^2$$

$$\Gamma = \frac{m\omega_0}{Q} \quad \left[\frac{kg}{s}\right]$$

{ Typical definition in force microscopy

Equivalent to:

$$\ddot{x} + \gamma\dot{x} + \omega_0^2 x = \frac{1}{m}F(t)$$

$$\gamma = \frac{\omega_0}{Q} \quad [Hz]$$

{ Typical definition in optomechanics

The energy lost from time $t=0$ to t is given by:

$$\Delta E = \int_{x(0)}^{x(t)} (-\Gamma\dot{x})\,dx = \int_0^t (-\Gamma\dot{x})\left(\frac{dx}{dt}\right)dt$$

$$\Delta E = \int_0^t (-\Gamma\dot{x}^2)\,dt$$

$-\Gamma\dot{x}^2$: rate of energy loss

$$\therefore \quad \frac{dE}{dt} = -\Gamma \dot{x}^2$$

The energy of the harmonic oscillator is:

$$E(t) = \frac{1}{2} m \dot{x}^2 + \frac{1}{2} k x^2$$

Using the solution to the harmonic oscillator equation of motion $x = x_0 e^{i\omega t}$, where $\omega = \sqrt{\frac{k}{m}} + i\frac{\Gamma}{2m} = \omega_0 + i\frac{\Gamma}{2m}$ and the system is dissipation is low $\frac{\Gamma}{2m} \ll \omega_0$:

$$E(t) = E_0 e^{-\frac{\Gamma}{m} t}$$

w/ $E_0 = \frac{1}{2} k x_0^2$

$$\therefore \quad \frac{dE}{dt} = -\frac{\Gamma}{m} E$$

← Recall the same formula in Lecture 10 in quantum definition of dissipation

This formula also allows us to understand the quality factor Q. Q is, in fact, sometimes defined as:

$$Q = 2\pi \frac{\text{Energy stored in oscillator}}{\text{Energy dissipated in one period}}$$

$$Q = 2\pi \frac{E}{\left(\frac{\Gamma}{m} E\right) T}$$

$$T = \frac{2\pi}{\omega_0}$$

$$\boxed{Q = \frac{m \omega_0}{\Gamma}}$$

↳ As before

$$\Gamma = \frac{m \omega_0}{Q}$$

II. Sources of Dissipation

Now that we have a clear idea of what Γ and Q represent, we should understand their origin in real nanomechanical resonators. As we already discussed these terms determine the fundamental sensitivity limits of nanomechanical sensors.

The total dissipation in a resonator is the sum of dissipation from various sources:

$$\Gamma = \Gamma_{medium} + \Gamma_{clamping} + \Gamma_{intrinsic} + \Gamma_{other}$$

- Γ_{medium}: losses due to interactions w/ fluid or ballistic medium
- $\Gamma_{clamping}$: energy radiating into environment through clamping point
- $\Gamma_{intrinsic}$: losses within the resonator itself
- Γ_{other}: the rest...

Equivalently, we can write this in terms of Q:

$$\frac{1}{Q} = \frac{1}{Q_{medium}} + \frac{1}{Q_{clamping}} + \frac{1}{Q_{intrinsic}} + \frac{1}{Q_{other}}$$

- Medium Dissipation

This dissipation depends on the medium surrounding the resonator, i.e. either a liquid or gas. The highest sensitivity applications are carried out in high vacuum, in which $\Gamma_{medium} = 0$.

In general, in a gas, there are two regimes: the **fluidic regime** and the **ballistic regime**. The value of the Knudsen number sets which regime applies to the system:

$$K = \frac{\lambda_f}{L},$$

where λ_f is the mean free path of the gas and L is the representative physical length scale of the resonator. If $K < 1$ ($\lambda_f < L$), the the system is in the fluidic regime. If $K > 1$ ($\lambda_f > L$), then the system is in the ballistic regime. In air at atmospheric pressure, $K = 1$ for

$L \approx 70$ nm.

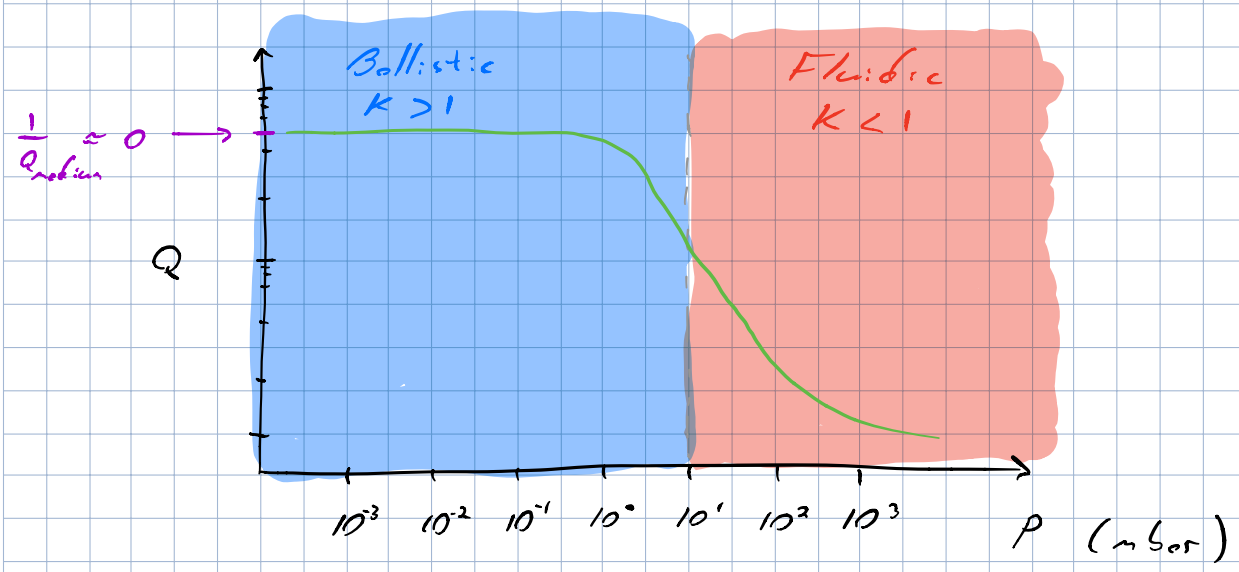

This line can be shifted to higher pressures for smaller resonators.

Therefore to reduce $\Gamma_{radiation}$, one should minimize the pressure and the size of the resonator.

- Clamping Dissipation

This mechanism describes losses due to the radiation of vibrational energy through the resonators anchoring point to the environment. In general, the clamping points needs to be designed in order to minimize such radiative losses, if this term is to

be made negligible.

In the specific case of cantilever beams, $\Gamma_{clamping}$ is minimized for long and thin beams clamped to a semi-infinite body.

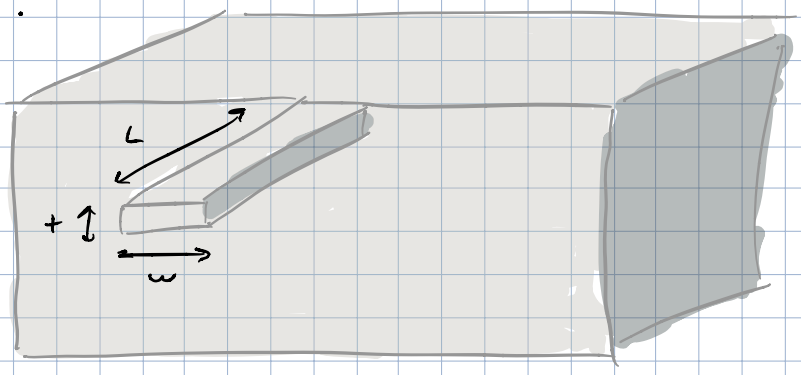

minimize: t, w

maximize: L

For membranes, a successful way to suppress radiation losses is to locate the vibrating structure within an appropriately designed phononic band-gap structure. This will remove free frame modes around the membrane, suppressing radiation loss.

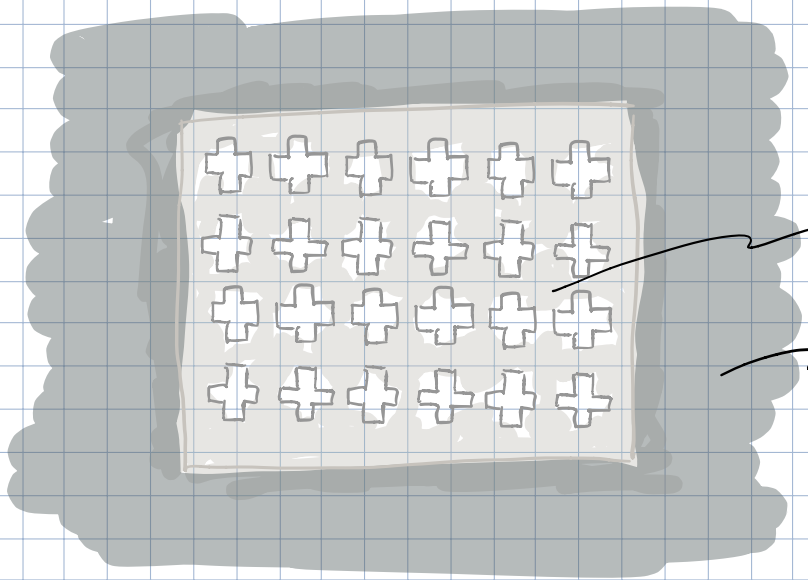

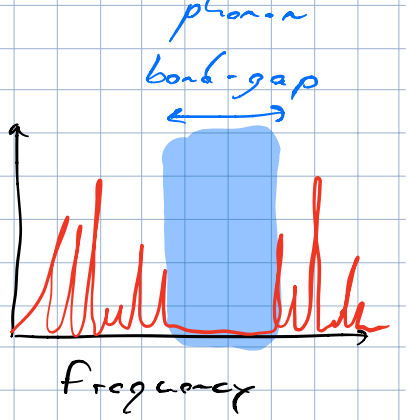

A phononic bandgap shield for high-*Q* membrane microresonators

P.-L. Yu,[1,2] K. Cicak,[3] N. S. Kampel,[1,2] Y. Tsaturyan,[1,2,a)] T. P. Purdy,[1,2] R. W. Simmonds,[3] and C. A. Regal[1,2,b)]

[1]*JILA, University of Colorado and National Institute of Standards and Technology, Boulder, Colorado 80309, USA*
[2]*Department of Physics, University of Colorado, Boulder, Colorado 80309, USA*
[3]*National Institute of Standards and Technology, Boulder, Colorado 80305, USA*

(Received 2 December 2013; accepted 31 December 2013; published online 15 January 2014)

A phononic crystal can control the acoustic coupling between a resonator and its support structure. We micromachine a phononic bandgap shield for high Q silicon nitride membranes and study the driven displacement spectra of the membranes and their support structures. We find that inside the observed bandgaps, the density and amplitude of non-membrane modes are greatly suppressed, and membrane modes are shielded from an external mechanical drive by up to 30 dB.
 [http://dx.doi.org/10.1063/1.4862031]

Micro- and nano-mechanical resonators offer great potential for precision sensing and realizing non-classical states of relatively massive objects.[1–4] One promising platform is silicon nitride (Si_3N_4) membrane resonators on silicon substrates,[5–7] in which large tensile stress results in a Q-frequency product above 10^{13} Hz.[8–10] Coupling these high-Q membranes to a Fabry-Pérot cavity has enabled quantum measurements on macroscopic objects and preparing mechanical modes close to the quantum ground state.[11–14]

Currently, an important limitation to the displacement sensitivity and radiation pressure effects of Si_3N_4 membranes in an optical cavity comes from the coupling between the membrane and the support structure.[10,15–17] This coupling results in (1) radiation loss, in which the energy of membrane modes radiates into the substrate, and (2) substrate noise, in which the mechanical modes of the silicon frame limit the optomechanical cooling. Thus far, the radiation loss in these devices has been addressed mainly by varying the techniques for grasping the silicon frame.[7,12,18] However, more sophisticated techniques for control of acoustic waves have been extensively studied in the field of acoustic metamaterials. In particular, a phononic crystal (PnC) with acoustic bandgaps can be used to filter or confine acoustic waves.[19–23] The use of PnC bandgaps to suppress the radiation loss of gigahertz, in-plane resonators has been demonstrated in the fields of microelectromechanical systems (MEMS) and optomechanics.[2,24]

In this work, we demonstrate a high-tension membrane inside of a silicon PnC structure that provides a shield for acoustic modes at megahertz frequencies. We probe the membrane modes and the non-membrane modes by measuring the displacement spectra of the membrane and different components of the support structure. We find that inside the observed bandgaps, the density and the amplitude of the non-membrane modes are greatly suppressed. In addition, the membrane modes, inside the observed bandgap, are shielded from an external mechanical drive by up to 30 dB.

The device consists of a patterned silicon substrate with a center island that contains high-tension square film of Si_3N_4 suspended across a mm-scale frame [Fig. 1(a)]. The unit cell length scale required to create a bandgap centered at a frequency f can be estimated by $\lambda/2 = v/2f \sim 1$ mm, where λ and v are the acoustic wavelength and velocity in silicon, respectively. For bandgaps centered at megahertz frequencies, we can fit three to four unit cells around the membrane with a 1 cm square chip. Our unit cell is composed of a square block with four bridges [Fig. 1(c)].[25,26]

We study two different devices (A and B) with different PnC shields [Fig. 1(a)], and a reference device (C) without the PnC shield. (see Table I for measured geometry parameters.) In Figs. 2(a) and 2(b), we display the band diagrams for the two different PnCs with infinite number of unit cells; this calculation is completed with the finite-element-method (FEM) software COMSOL using the measured device parameters.

Fabrication of the devices begins with the growth of a 100-nm-thick Si_3N_4 film by low-pressure chemical vapor

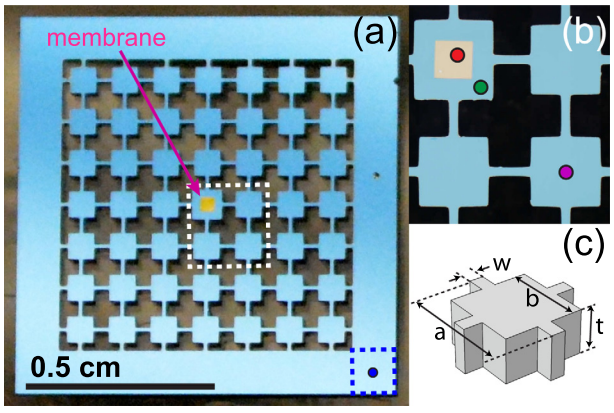

FIG. 1. (a) Photograph of device A. The chip frame (CF) is connected to the piezoelectric actuator at four corners (the blue dashed region). (b) Expanded view of the white dashed regions shows a square membrane (M, yellow) surrounded by a membrane frame (MF, light blue) and a PnC unit cell (PnC, light blue). The red, green, and purple spots in (b) and the blue spot in (a) are locations of displacement measurements in Figs. 2(c)–2(f). (c) Schematic of the PnC unit cell and definitions of the geometry parameters. See Table I for the values of these parameters for the devices A and B.

a)Current address: QUANTOP, Niels Bohr Institute, University of Copenhagen, Blegdamsvej 17, 2100 Copenhagen, Denmark.
b)Electronic mail: regal@colorado.edu

TABLE I. Measured geometry parameters of the devices.

Definition [μm]	Symbol	Device A	Device B	Device C[a]
Number of unit cells[b]		3	4.5	…
Unit cell size	a	1100 μm	800 μm	…
Block length	b	686	542	..
Bridge width	w	97	96	…
Wafer thickness	t	300	300	…
Membrane length	l	372	367	500
Membrane frame size		786	783	10^4
Membrane thickness		0.1	0.1	0.04

[a]Norcada, Inc.
[b]Between the center and the edge of the chip.

deposition on both sides of a 300-μm thick Si wafer. The membrane and PnC structure are created in two sequential steps; each starts with patterned removal of the back Si_3N_4 layer followed by deep reactive-ion etching (DRIE) for bulk Si machining. In the first step, the DRIE stops tens of microns short of etching fully through the wafer, and a KOH wet etch completes the release of the square Si_3N_4 membrane on the front of the wafer. In the second step, the PnC crosses are micromachined with DRIE all the way through the wafer (resulting in PnC holes that are vertical to $\sim 1^\circ$). During fabrication (except the KOH step), the front side of the wafer is glued with processing adhesive to a protection substrate, and the final devices are released from the protection substrate and cleaned using solvents and a sulfuric-acid-based solution.

The membrane resonator vibrates like a drum with discrete frequencies given by $f_{mn} = \sqrt{\sigma(m^2+n^2)/4\rho l^2}$, where σ is the tensile stress, (m,n) are integer mode indices representing the number of antinodes, ρ is the volume mass density, and l is the membrane side length. The fabricated membranes in the PnCs are experimentally confirmed to be under a high tensile stress of 1 GPa: The fundamental membrane frequency for devices A and B is 1.1 MHz.

To characterize the mechanical properties of the devices, we excite the chip at different frequencies through a piezoelectric ring actuator connected to all four frame corners with double-sided tape and measure displacement using a Mach-Zehnder interferometer. First, we present studies in which we probe the displacement of the Si_3N_4 membrane. We position the optical spot slightly off the membrane center to allow a variety of modes to be probed. The driven displacements as a function of frequency for devices A and B are compared with that of a control device C in Figs. 2(c) and 2(d), respectively. We find that the displacement is clearly suppressed in the frequency ranges of 1.5–2.75 MHz and 4.05–4.45 MHz (2.65–3.25 MHz and 3.5–4.5 MHz) for device A (B), resulting in a flat response that is limited by the shot noise of optical detection. These "observed bandgaps" roughly overlap with the calculated bandgaps [grey regions in both Figs. 2(a),2(b) and 2(c),2(d)]. The center frequencies of the observed and predicted bandgaps are consistent within $\sim 10\%$.

Most of the modes we see in Figs. 2(c) and 2(d) are non-membrane modes; the finite number of membrane modes is shown by dashed lines. Physically, the chip consists of (1) the membrane (M), (2) the membrane frame (MF), (3) the PnC structure (PnC), and (4) the chip frame (CF) [Fig. 1(a)]. The membrane and the MF together form a "defect" embedded in the PnC lattice. We optically probe the MF, the PnC, and the CF by focusing on the three different locations indicated in Fig. 1(b). Looking at these spectra in conjunction with the membrane displacement, we can understand the origin of the non-membrane modes. The piezoelectric actuator itself has frequency-dependent structure, and measuring at

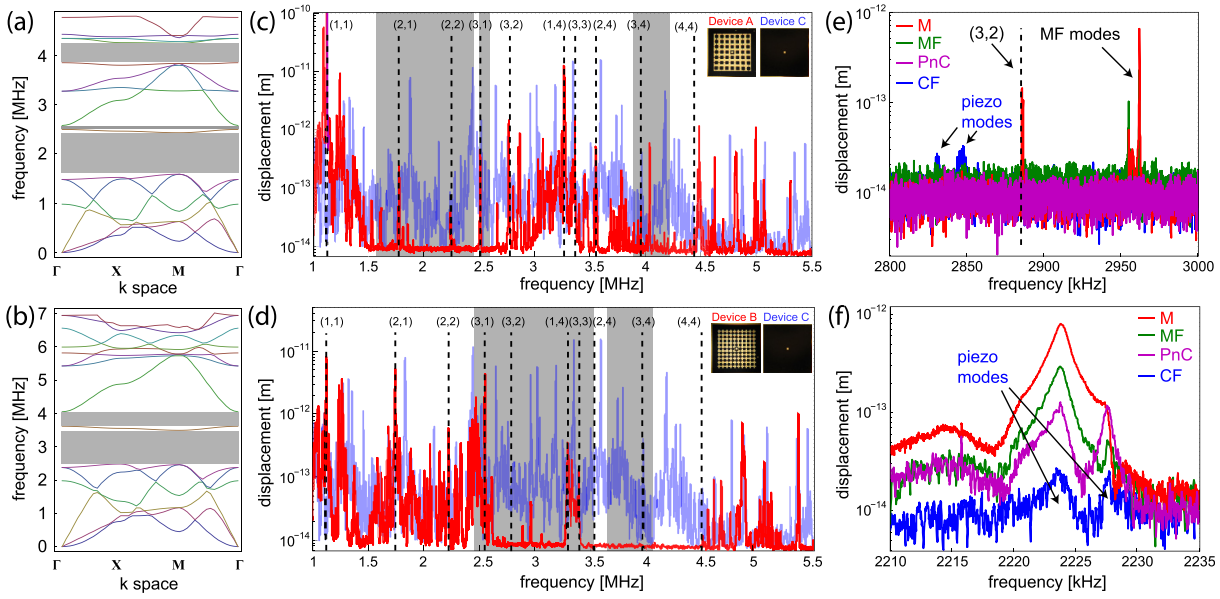

FIG. 2. Frequency-dependent mechanical response. (a) and (b) Simulated band diagrams for infinite number of the unit cells used in devices A and B. Bandgap ranges are shown in grey. (c) and (d) Measured membrane displacement spectra of devices A, B, and C. The data are smoothed with a 4 kHz bandwidth. The ranges of ideal bandgaps are shown in grey. Membrane modes predicted based on the observed fundamental mode frequencies of devices A and B (up to the (4,4) mode) are shown by dashed lines. (e) and (f) Probing the non-membrane modes via measuring displacement spectra at different locations on device B: At the membrane (red), the membrane frame (MF, green), the PnC (purple), and the corner of chip frame (CF, blue). (e) An example spectral region in an observed bandgap in device B. (f) An example of two non-membrane modes of device B outside the observed bandgaps.

the CF reveals the information about this structure. Mainly, the displacement measured on the corner of CF is limited by the detection noise, but some "piezo-modes" are clearly identifiable [see Figs. 2(e) and 2(f) for two examples].

We find that the combined spectra have distinct features inside and outside the observed bandgaps. Inside the observed bandgap, the spectra of the PnC, the MF, and the membrane are flat except a couple of "defect modes" observed in the spectra of the MF and the membrane [see Fig. 2(e) for one example]. While the mechanical modes of the MF cannot be completely avoided in the bandgap, they only occur sparsely and are clearly separable from the membrane modes. Outside the observed bandgaps, most modes except the membrane modes have comparable motion in the membrane, the MF, and the PnC [see Fig. 2(f) for one example]. We also find that piezo modes greatly enhance the motion of other components, while inside the observed bandgaps the piezo modes do not induce any observed motion of other components [compare Figs. 2(f) and 2(e)].

The observed eigenmodes include admixtures of modes created by the membrane, the MF, the PnC, and the CF. We use a FEM to simulate the whole device in order to visualize and characterize the expected frequency-dependent structure of all the modes. The boundary conditions for the simulation fix the corners of the back side of the chip. We find all the eigenmodes between 1 and 5 MHz. To estimate the motion that will be observed on the Si_3N_4 membrane [as measured in Figs. 2(c) and 2(d)], for each mode we calculate a "partition coefficient" defined by the ratio of the energy stored in the membrane to the energy stored in the whole device

$$\mathcal{E}_{\text{mem}} \equiv \frac{\int_{\text{mem}} \varrho(\mathbf{x})|\mathbf{u}(\mathbf{x})|^2 d^3x}{\int_{\text{whole}} \varrho(\mathbf{x})|\mathbf{u}(\mathbf{x})|^2 d^3x}, \tag{1}$$

where $\mathbf{u}(\mathbf{x})$ is the simulated displacement field and $\varrho(\mathbf{x})$ is the mass density field.

The partition coefficient $\mathcal{E}_{\text{mem}}$ is plotted in Fig. 3 as a function of mode frequency using the parameters for devices B and C. The membrane modes are clearly identifiable as the $\mathcal{E}_{\text{mem}} \simeq 0$ dB; these modes have the small effective mass associated with the Si_3N_4 membrane. A majority of the non-membrane modes of device C have an $\mathcal{E}_{\text{mem}}$ between -40 and -60 dB; these modes have a much larger effective mass associated with the silicon substrate. For device B, there are two ranges with reduced $\mathcal{E}_{\text{mem}}$ that roughly overlap with the ideal calculated bandgaps. The reductions are finite ($\mathcal{E}_{\text{mem}}$ between -70 and -130 dB) and smoothly degraded because the simulation takes into account the finite number of unit cells. There are also a finite number of non-membrane modes with $\mathcal{E}_{\text{mem}} > -40$ dB. Inside the device-B bandgap, these modes can be classified as defect modes with $\mathcal{E}_{\text{mem}} < -30$ dB. Outside of the device-B bandgap and in device C, there are a larger number of modes ($\sim$4% of the modes) with $\mathcal{E}_{\text{mem}} > -40$ dB. These modes with the largest $\mathcal{E}_{\text{mem}}$ tend to be clustered near the expected membrane mode frequencies.

In Figs. 3(b)–3(f), we also show the displacement profile of example modes on a logarithmic scale. We see that the non-membrane modes inside the bandgaps are dominated by the MF or the CF, and the displacement field decays exponentially in the PnC [Figs. 3(c) and 3(d)]. On the contrary, the non-membrane modes outside the bandgaps have a uniformly distributed displacement field [Fig. 3(b)]. We also find that for the membrane modes inside and outside the bandgaps [Figs. 3(e) and 3(f)], the displacement fields in the PnC behave the same as the non-membrane modes inside and outside the bandgaps. In other words, inside the bandgap, the PnC acts as a passive mechanical filter that decouples the CF and the "defect;" outside the bandgap, the PnC moves with all the other components together, i.e., they can be strongly coupled.

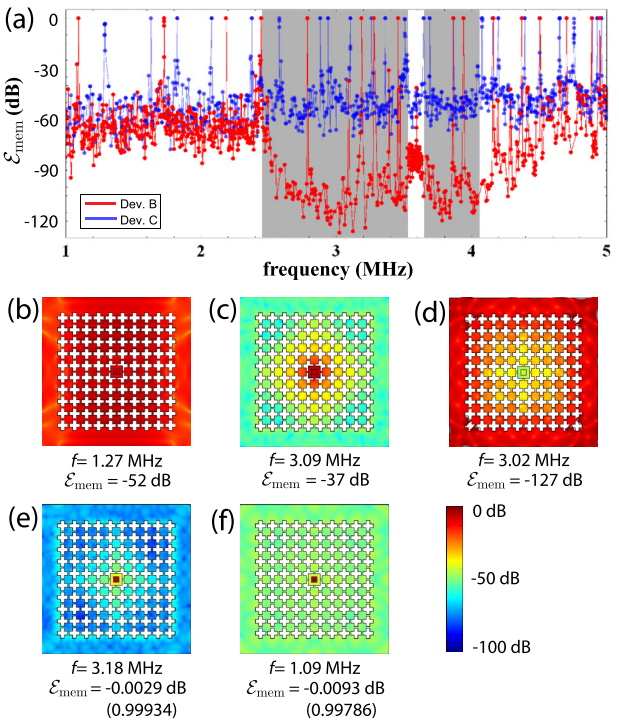

FIG. 3. Simulated membrane and non-membrane modes for devices B and C. (a) Simulated partition coefficient $\mathcal{E}_{\text{mem}}$ of devices B and C. Data of device B (C) are red (blue). Data of each device are connected by lines to see the trend. Ideal calculated bandgaps are shown in grey. (b)–(f) Simulated displacement field for four kinds of modes. Color scheme represents the amplitude of displacement in a logarithmic scale. (b) An example of a non-membrane mode outside the bandgap. (c) An example of a MF mode inside the bandgap. (d) An example of a CF mode inside the bandgap. (e) and (f) Two examples of membrane modes inside/outside the bandgap.

Finally, we have studied the efficiency with which the piezoelectric actuator can drive membrane modes inside and outside the bandgap. The piezoelectric actuator does not directly drive the membrane; it drives the membrane through the chip frame, the PnC, and the membrane frame. In other words, the piezoelectric actuator actuates the membrane mode through the non-membrane modes, and hence, we expect the driving efficiency to be low inside the observed bandgap. We quantitatively analyze this effect by measuring the piezo actuated energy of the (1,1) through (4,4) membrane modes of devices A and C. To obtain a calibrated measure of the relative actuated energy, we also measure for each mode the thermally actuated energy provided by the thermal fluctuating force, which is not shielded by the PnC. The ratio of the driven to thermal energy, R, can be obtained by comparing the driven to thermal vibration amplitude

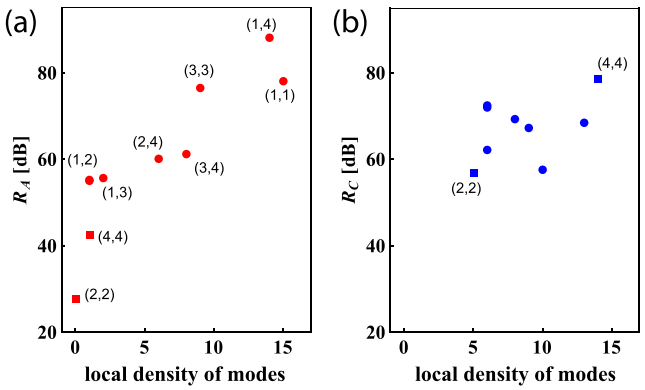

FIG. 4. The ratio of the actuated energy of the membrane modes provided by the piezoelectric actuator to that by the thermal fluctuating force as a function of a local density of modes. The density is determined from the data in Fig. 1(c) by counting the number of observed modes in a 50 kHz range centered at each membrane mode. (a) Data for device A. The membrane mode indices are labeled. (b) Data for device C. The corresponding modes with lowest R in (a) are shown in square.

$$R = R(p,f,B_w) \propto \frac{|\mathcal{D}(p,f)/\eta|^2}{[\mathcal{S}_d(f)/\eta^2]B_w} = \frac{|\mathcal{D}(p,f)|^2}{\mathcal{S}_d(f)B_w}, \qquad (2)$$

where $\mathcal{D}(p,f)$ is the driven displacement amplitude measured with a network analyzer under external driving power p, $\mathcal{S}_d(f)$ is the displacement spectral density measured with a spectrum analyzer without external driving power, η is the overlap factor between the optical spot and the membrane mode shape, and $B_w = 2$ Hz is the resolution bandwidth of the spectrum analyzer.

In Fig. 4, we plot R as a function of a measure that approximates the local mode density near each membrane mode. This measure provides an estimate of the expected driving efficiency, but not necessarily a rigorous correspondence, because the set of optically measured modes will not necessarily correspond to the set of modes that couple best to a particular membrane mode. Nonetheless, we see a positive correlation between the driven motion and this mode density for device A. We also observe a much larger dynamic range in R for device A than for device C, which is as expected because the phononic crystal structure introduces a nonuniformity to the local mode structure. A direct comparison between devices A and C shows the smallest R in device A is 30 dB smaller than the smallest R in device C, indicating that in the bandgap membrane modes can be significantly isolated from the chip frame.

Delivering energy from the chip frame to the membrane is the reverse process of radiating energy from the membrane to the chip frame. Therefore, the well-isolated (small R) membrane modes are expected to have small radiation loss. However, the highest Q of the membrane modes we observed in device A is about 10^6, comparable with the highest Q of the membrane modes in device C. This is possibly because the membranes are still limited by the material loss. In fact, in this new fabrication process, we know that some defects were generated; images of some of the membranes reveal inhomogeneous spots up to 100 μm in size. In the future, we will investigate realizing higher Si_3N_4 Qs in the bandgaps by measuring at cryogenic temperature and improving control of the fabrication.

We thank K. W. Lehnert, S. B. Papp, R. W. Andrews, and Y.-P. Huang for valuable discussions, and J. A. Beall for helpful discussions on device fabrication. This work was supported by the DARPA QuASAR program, the ONR YIP, and the National Science Foundation under Grant No. 1125844. C.R. thanks the Clare Boothe Luce Foundation for support. P.-L.Y. thanks the Taiwan Ministry of Education for support.

[1]A. D. O'Connell, M. Hofheinz, M. Ansmann, R. C. Bialczak, M. Lenander, E. Lucero, M. Neeley, D. Sank, H. Wang, M. Weides, J. Wenner, J. M. Martinis, and A. N. Cleland, Nature **464**, 697 (2010).
[2]J. Chan, T. P. M. Alegre, A. H. Safavi-Naeini, J. T. Hill, A. Krause, S. Groeblacher, M. Aspelmeyer, and O. Painter, Nature **478**, 89 (2011).
[3]J. D. Teufel, T. Donner, D. Li, J. W. Harlow, M. S. Allman, K. Cicak, A. J. Sirois, J. D. Whittaker, K. W. Lehnert, and R. W. Simmonds, Nature **475**, 359 (2011).
[4]T. A. Palomaki, J. D. Teufel, R. W. Simmonds, and K. W. Lehnert, Science **342**, 710 (2013).
[5]S. S. Verbridge, J. M. Parpia, R. B. Reichenbach, L. M. Bellan, and H. G. Craighead, J. Appl. Phys. **99**, 124304 (2006).
[6]B. M. Zwickl, W. E. Shanks, A. M. Jayich, C. Yang, A. C. Bleszynski Jayich, J. D. Thompson, and J. G. E. Harris, Appl. Phys. Lett. **92**, 103125 (2008).
[7]D. J. Wilson, C. A. Regal, S. B. Papp, and H. J. Kimble, Phys. Rev. Lett. **103**, 207204 (2009).
[8]Q. P. Unterreithmeier, T. Faust, and J. P. Kotthaus, Phys. Rev. Lett. **105**, 027205 (2010).
[9]S. Schmid, K. D. Jensen, K. H. Nielsen, and A. Boisen, Phys. Rev. B **84**, 165307 (2011).
[10]P.-L. Yu, T. P. Purdy, and C. A. Regal, Phys. Rev. Lett. **108**, 083603 (2012).
[11]J. D. Thompson, B. M. Zwickl, A. M. Jayich, F. Marquardt, S. M. Girvin, and J. G. E. Harris, Nature **452**, 72 (2008).
[12]T. P. Purdy, R. W. Peterson, P.-L. Yu, and C. A. Regal, New J. Phys. **14**, 115021 (2012).
[13]T. P. Purdy, R. W. Peterson, and C. A. Regal, Science **339**, 801 (2013).
[14]T. P. Purdy, P.-L. Yu, R. W. Peterson, N. S. Kampel, and C. A. Regal, Phys. Rev. X **3**, 031012 (2013).
[15]A. Jockel, M. T. Rakher, M. Korppi, S. Camerer, D. Hunger, M. Mader, and P. Treutlein, Appl. Phys. Lett. **99**, 143109 (2011).
[16]I. Wilson-Rae, R. A. Barton, S. S. Verbridge, D. R. Southworth, B. Ilic, H. G. Craighead, and J. M. Parpia, Phys. Rev. Lett. **106**, 047205 (2011).
[17]P.-L. Yu, T. P. Purdy, G. D. Cole, and C. A. Regal, CLEO: Science and Innovations (OSA Technical Digest), Paper No. CW3F.8, 2013.
[18]B. M. Zwickl, Ph.D. dissertation, Yale University, 2011.
[19]V. Narayanamurti, H. L. Störmer, M. A. Chin, A. C. Gossard, and W. Wiegmann, Phys. Rev. Lett. **43**, 2012 (1979).
[20]M. M. Sigalas and E. N. Economou, J. Sound Vib. **158**, 377 (1992).
[21]M. S. Kushwaha, P. Halevi, L. Dobrzynski, and B. Djafari-Rouhani, Phys. Rev. Lett. **71**, 2022 (1993).
[22]R. Martínez-Sala, J. Sancho, J. V. Sánchez, V. Gómez, J. Llinares, and F. Meseguer, Nature **378**, 241 (1995).
[23]M. Maldovan, Nature **503**, 209 (2013).
[24]S. Mohammadi, A. A. Eftekhar, W. D. Hunt, and A. Adibi, Appl. Phys. Lett. **94**, 051906 (2009).
[25]A. H. Safavi-Naeini and O. Painter, Opt. Express **18**, 14926 (2010).
[26]T. P. M. Alegre, A. Safavi-Naeini, M. Winger, and O. Painter, Opt. Express **19**, 5658 (2011).

- Intrinsic Dissipation

This category includes all energy losses that take place within or on the mechanical resonator. These losses can be divided into **frictional losses** and **fundamental losses**.

frictional losses: from material imperfections in the bulk or on the surface

fundamental losses: losses occurring even in an ideal frictionless material due to phonons and electrons

Frictional losses come from irreversible motion of atoms during vibration, e.g. from defect dislocations in a crystal, grain boundary slipping in a metal, phase boundary slipping in layered structures, or molecular chain motion in an amorphous solid. Such losses can be described by Zener's model for an anelastic solid, which we discussed in Lecture 2. There we introduced the possibility of time lag in the stress-strain relationship. Ultimately this resulted in a frequency dependent Q:

$$\frac{1}{Q_{Friction}} = \frac{\omega T}{1+\omega^2 T^2}\,\Delta \quad \text{w/} \quad T = \sqrt{T_\sigma T_\varepsilon} \quad \text{and} \quad \Delta = \frac{T_\sigma - T_\varepsilon}{T}$$

where T_σ and T_ε are the relaxation times at constant stress and strain, respectively.

This results in a frictional dissipation (proportional to $\frac{1}{Q_{Friction}}$) peaked at $\omega = \frac{1}{T}$.

Fundamental losses include thermoelastic loss and phonon-phonon interaction loss. Like frictional loss, both can be modelled by Zener's approach and therefore have a similar dependence on ω.

Thermoelastic loss → Mechanical motion generates local differences in temperature and therefore heat flow between these points. This process results in dissipation of energy.

Phonon-phonon loss → Oscillating strain field changes normal mode

frequencies of atomic vibrations in a crystal. Temperature differences in these normal modes results in heat flow and energy loss.

- Other Dissipation

This term includes all remaining losses, including dissipation due to electrical charges trapped on the resonator, eddy current damping, magnetic dissipation due to magnetic impurities, etc.

III. Damping Dilution

In recent years a scheme for achieving very high Q resonators has been developed for strings and membranes. In a cantilever, the energy stored and lost over an oscillation cycle is related to its bending. For strings and membranes, energy can also be stored and lost in

lateral elongation. Also strings and membranes can build up a lot of potential energy when vibrational deflection works against high lateral tensile stress.

stored energy per cycle

$$Q = 2\pi \frac{W_{tension} + W_{elongation} + W_{bending}}{\Delta W_{elongation} + \Delta W_{bending}}$$

lost energy per cycle

We increase the tension to increase the stored energy w/o increasing loss.

Let $Q_{intrinsic} = 2\pi \frac{W_e + W_b}{\Delta W_e + \Delta W_b}$, then:

$$Q = \frac{W_t + W_e + W_b}{W_e + W_b} \cdot Q_{intrinsic}$$

If we increase the tension such that $W_t >> W_e, W_b$:

$$Q \approx \frac{W_t}{W_e + W_b} \cdot Q_{intrinsic}$$

$$Q \approx \alpha_{dd} \cdot Q_{intrinsic}$$

If very small, α_{dd} can be large.

where $$\alpha_{dd} = \left[\frac{W_e}{W_+} + \frac{W_b}{W_+} \right]^{-1}$$

Damping Dilution factor

For both strings and membranes one can calculate the energy stored in elongation, bending, and torsion from the mode slopes (see Fund. Nanomech. Resonators, p. 81 - 87). In both cases $\frac{W_b}{W_+}$ is independent of the vibrational amplitude, while $\frac{W_e}{W_+}$ depends on the square of the ratio between the vibrational amplitude and the resonator thickness. Since in most cases the amplitude is much smaller than the thickness, we have:

$$\frac{W_b}{W_+} >> \frac{W_e}{W_+}$$

$$\therefore \quad \alpha_{dd} \approx \left[\frac{W_b}{W_+} \right]^{-1}$$

↓

This ratio can be separated into two terms

$$\alpha_{dd} \approx \left[c_1 \left(\frac{h}{L}\right)^2 + c_2 \left(\frac{h}{L}\right) \right]^{-1}$$

bending at center

bending at edge

c_1 and c_2 are constants depending on the mode number, geometry, and material. h is the thickness of the string or membrane and L is its lateral dimension (length for a string; length and width for a membrane).

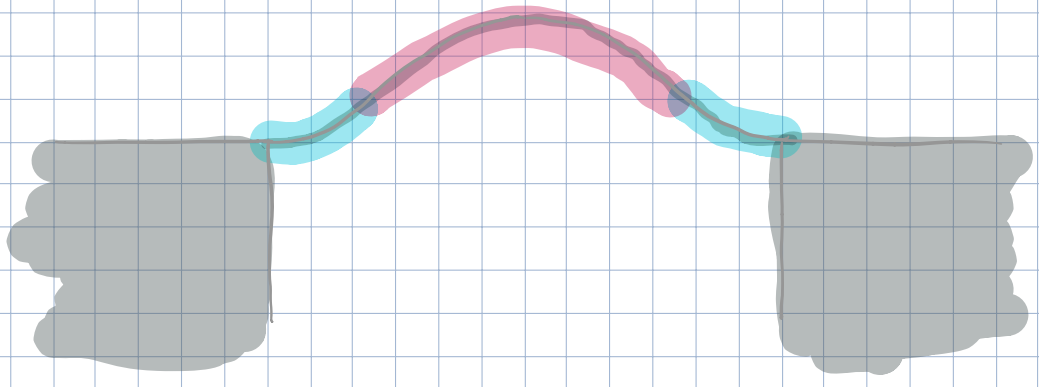

Given that $\frac{h}{L} << 1$, the bending at the edge dominates this effect. Therefore, in order to obtain the highest possible

Q, one should apply high tension and minimize bending of the resonator near the clamping points, i.e. realize "soft clamping".

Note: damping dilution increases Q which is useful for frequency standards and optomechanics. It does not decrease Γ. Recall that $\Gamma = \frac{m\omega_0}{Q}$. Increasing tension, increases stored energy and also the resonant frequency: $\omega_0 \propto W_t$. Damping dilution gives $Q \propto W_t$ as well.

$$\therefore \Gamma = \frac{m\omega_0}{Q} \propto \frac{W_t}{W_t}$$

$$\Gamma \propto (W_t)^0$$

Independent of tension

Therefore, for example, force and torque sensitivity cannot be improved by damping dilution.

REPORT

QUANTUM MATERIALS

Elastic strain engineering for ultralow mechanical dissipation

A. H. Ghadimi,[1]* S. A. Fedorov,[1]* N. J. Engelsen,[1]* M. J. Bereyhi,[1] R. Schilling,[1] D. J. Wilson,[2]† T. J. Kippenberg[1]†

Extreme stresses can be produced in nanoscale structures; this feature has been used to realize enhanced materials properties, such as the high mobility of silicon in modern transistors. We show how nanoscale stress can be used to realize exceptionally low mechanical dissipation when combined with "soft-clamping"—a form of phononic engineering. Specifically, using a nonuniform phononic crystal pattern, we colocalize the strain and flexural motion of a free-standing silicon nitride nanobeam. Ringdown measurements at room temperature reveal string-like vibrational modes with quality (*Q*) factors as high as 800 million and *Q* × frequency exceeding 10^{15} hertz. These results illustrate a promising route for engineering ultracoherent nanomechanical devices.

Elastic strain engineering uses stress to realize unusual material properties (*1*). For instance, stress can enhance the electron mobility of a semiconductor, enabling more efficient solar cells (*2*) and smaller, faster transistors (*3*). In mechanical engineering, the pursuit of resonators with low dissipation (*4*) has led to studies of a complementary strain engineering technique known as dissipation dilution, whereby the stiffness of a stressed material is effectively increased without added loss (*5*–*8*). Unlike most bulk mechanical properties, dissipation dilution can improve with reduced device dimensions, implying that smaller-mass resonators can have higher quality factors *Q*. This unusual scaling is responsible for the anomalously high *Q* of Si_3N_4 nanomechanical resonators (*8*–*11*) and has led to the emergence of "quantum-coherent" resonators with thermal decoherence times $\hbar Q/k_B T$ longer than one vibrational period (where $\hbar$, k_B, and T are the reduced Planck constant, Boltzmann constant, and bath temperature, respectively).

Whereas elastic strain engineering commonly relies on extreme inhomogeneous stresses produced by nanoscale deformation (*12*) [e.g., by lithographic patterning (*13*, *14*) or nano-indentation (*15*)], nearly all studies of dissipation dilution have focused on materials under weak, uniform stress produced during material synthesis. The main challenge in bridging these two approaches is to identify strategies to colocalize stress and mechanical motion at the nanoscale. Our strategy, based on phononic crystal patterning, is conceptually simple and entirely material-independent (Fig. 1): By weakly corrugating a prestressed nanobeam, we create a band gap for localizing its flexural modes around a central defect. By tapering the beam, we colocalize these modes with a region of enhanced stress. Reduced motion near the supports ["soft-clamping" (*8*)] results in higher dissipation dilution, while enhanced stress increases both dilution and mode frequency. We implemented this approach on tapered beams with extremely high aspect ratios (as long as 7 mm and as thin as 20 nm) made of 1.1 GPa–prestressed Si_3N_4, and achieved local stresses as high as 3.8 GPa.

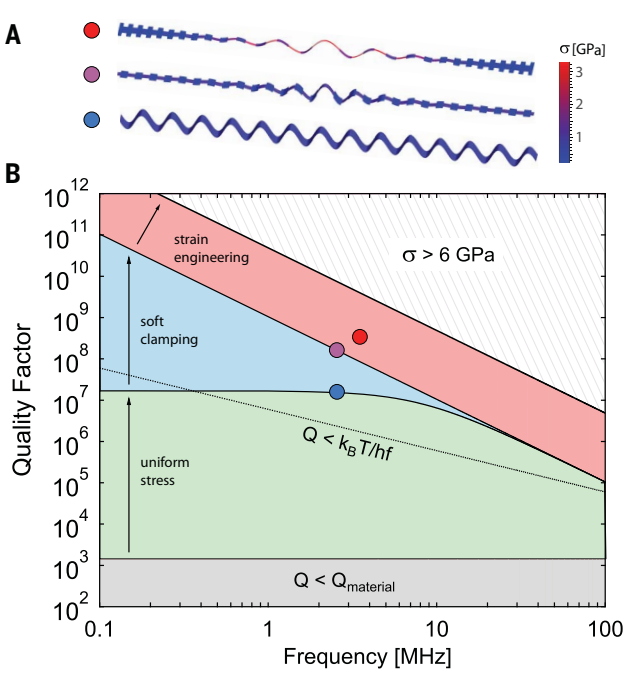

Fig. 1. Ultrahigh-*Q* nanobeams through dissipation dilution. (**A**) Mode shapes representing three strategies to enhance the *Q* of a nanobeam via dissipation dilution. From bottom to top: uniform stress, soft-clamping, and geometric strain engineering. Color scale represents axial stress σ. (**B**) *Q* versus mode frequency (*f*) accessible for a 20-nm-thick Si_3N_4 nanobeam, following Eq. 3. Gray region: *Q*(*f*) of an unstressed beam, limited by material loss. Green region: *Q*(*f*) of a 3-mm-long uniform beam with σ < 1 GPa. Blue region: *Q*(*f*) accessible by soft-clamping. Red region: *Q*(*f*) accessible by soft-clamping and strain engineering. Hatched region (upper right) is forbidden by the material yield strength. Solid circles correspond to measurements described in the main text.

To illustrate the basic features of our approach, we first consider a model for dissipation dilution of a nonuniform beam of length L, thickness h, and variable width $w(x)$. Following an anelastic approach successfully applied to uniform nanobeams (*6*, *7*) and nanomembranes (*16*), we partition the potential energy of the beam U into two components: a dissipative component due to bending, $U_E = \frac{1}{2} E_0 \int_0^L I(x)[u''(x)]^2 dx$, and a conservative component due to elongation, $U_\sigma = \frac{1}{2} T \int_0^L [u'(x)]^2 dx$, where $u(x)$ is the vibrational mode shape, $I(x) = (1/12) w(x) h^3$ is the geometric moment of inertia, E_0 is the Young's modulus, $\mathcal{T} = hw(x)\sigma(x)$ is the tension, and $\sigma(x)$ is the axial stress of the beam, respectively. The *Q* enhancement due to stress (the dissipation "dilution factor") is given by the participation ratio of the lossy potential (*5*–*7*):

$$\frac{Q}{Q_0} = 1 + \frac{U_\sigma}{U_E} \approx \frac{12}{E_0 h^2} \cdot \frac{\int_0^L [u'(x)]^2 dx}{\int_0^L \sigma^{-1}(x)[u''(x)]^2 dx} \quad (1)$$

where Q_0 is the intrinsic (undiluted) quality factor. For the familiar case of a uniform beam with a string-like mode shape described by $u(x) \propto \sin(\pi n x/L)$, where n is the mode number, Eq. 1 implies that

$$\frac{Q}{Q_0} \approx \frac{3}{\pi^2} \frac{\sigma^2}{E_0 h^2 \rho f^2} \quad (2)$$

where ρ is the material density and $f = (n/L)\sqrt{\sigma/\rho}$ is the mode frequency. Nearly all stressed nanomechanical resonators studied to date have operated far below this limit. The main reason for this discrepancy is clamping loss; for example, in the case of a doubly clamped beam, boundary

[1]Institute of Physics, École Polytechnique Fédérale de Lausanne, 1015 Lausanne, Switzerland. [2]IBM Research–Zurich, 8803 Rüschlikon, Switzerland.
*These authors contributed equally to this work.
†Corresponding author. Email: daw@zurich.ibm.com (D.J.W.); tobias.kippenberg@epfl.ch (T.J.K.)

conditions $u'(x_0) = u(x_0) = 0$ require that the vibrational mode shape exhibit extra curvature [$u''(x)$] near the supports ($x_0 = 0, L$), resulting in a reduced dilution factor of the form

$$\frac{Q}{Q_0} \approx \left(\underbrace{2\lambda}_{\text{supports}} + \underbrace{\pi^2 n^2 \lambda^2}_{\text{antinodes}} \right)^{-1} \quad (3)$$

(*7*, *17*), where $\lambda = (h/L)\sqrt{1/(12\varepsilon)}$ in units of axial strain $\varepsilon = \sigma/E$.

The uniform beam model (Eq. 3) gives several rules of thumb for maximizing the Q (or $Q \times f$ product) of a stressed nanomechanical resonator; namely, Q is typically highest for the fundamental mode ($n = 1$) and can be increased by increasing the aspect ratio (L/h) or stress. By contrast, $Q \times f$ is typically larger for high-order modes. Both strategies have been explored for a wide variety of beam- and membrane-like geometries (*17*, *18*). A third approach, recently demonstrated with a membrane (*8*), is to use periodic micropatterning [a phononic crystal (PnC)] to localize the mode shape away from the supports. By this soft-clamping approach, the leading term in Eq. 3 can be suppressed, giving access to the performance of an ideal clamp-free resonator (Eq. 2).

Complementary to soft-clamping, our approach consists of colocalizing the mode shape with a region of geometrically enhanced stress, making use of the tension balance relation $\sigma(x) = T/[w(x)h]$ [similar to microbridge structures (*13*, *14*)]. Inhomogeneous stress has been exploited before to increase the $Q \times f$ product of a nanomechanical resonator (*19*); however, performance was in this case limited by rigid clamping. Combining geometrically enhanced stress with soft-clamping can lead to improved performance: For example, Eq. 2 suggests that the Q (for a fixed f) of a typical 1 GPa–prestressed Si_3N_4 nanobeam can be enhanced by a factor of 50 before the stress in the thinnest part of the beam reaches the yield strength of Si_3N_4 ($\sigma_{yield} \approx 6$ GPa). This material limit, described by Eq. 2 with $\sigma = \sigma_{yield}$ and illustrated by the hatched region in Fig. 1, can be shown to apply to an arbitrary beam profile $w(x)$ (*20*). In gaining access to it, the main caveat of our approach is the small area in which the stress is enhanced, which implies that high-order flexural modes must be used to achieve sufficient colocalization.

Devices were patterned on 20-nm-thick films of high-stress Si_3N_4 ($E_0 \approx 250$ GPa, $\sigma_0 \approx 1.1$ GPa) grown by low-pressure chemical vapor deposition on a Si wafer. A multistep release process (*20*) was used to suspend beams as long as 7 mm, enabling aspect ratios as high as 3.5×10^5 and dilution factors in excess of $(2\lambda)^{-1} \approx 3 \times 10^4$. PnCs were realized by corrugating beams with a simple step-like unit cell (length L_c, minor width w_{min}, major width $w_{max} \approx 2w_{min}$) (Fig. 2A). A uniform defect of length L_d was patterned at the center of each beam to define the position of localized modes. Colocalization of stress with these modes is achieved by adiabatically tapering the width of successive unit cells toward the defect according to a Gaussian envelope function (*20*).

Localized modes of PnC nanobeams ("1D phononic crystals") have already been widely studied, as their ultralow mass and sparse mode spectrum make them highly promising for sensing applications. However, in contrast to 2D (membrane-like) resonators (*8*), ultrahigh Q in 1D PnCs has not been reported to date because of a focus on unstrained materials (*21*) and/or highly confined (high-curvature) modes (*18*) limited by radiation loss. With this discrepancy in mind, we first embarked on a study of uniform (untapered) PnC nanobeams, focusing on localized modes of our high–aspect ratio devices.

An experiment demonstrating soft-clamped 1D nanomechanical resonators is shown in Fig. 3. We studied 2.6-mm-long devices with unit cells of length $L_c = 100$ μm and width $w_{min(max)} = 0.5 \pm 0.1$ μm. To characterize these devices, we carried out thermal noise and ringdown measurements in vacuo ($<10^{-6}$ mbar) using a lensed-fiber interferometer (*20*). As a consequence of their simple geometry, mode frequencies (inferred from thermal noise spectra; Fig. 3E) were found to agree well with a numerical solution to the 1D Euler-Bernoulli equation (*20*). Particularly striking is the sparse mode spectrum inside the band gap, visualized by compiling spectra of beams with different defect lengths (Fig. 3F). A single defect mode appears to move in and out of the band gap as the defect length is varied. This mode is expected to be localized and therefore to have a reduced effective mass m. Comparing the area under thermal noise peaks and estimating the physical beam mass to be $m_0 = 100$ pg, we infer that indeed $m \approx 5$ pg $<< m_0$ (*20*). This value is in good agreement with the mode profile obtained from the Euler-Bernoulli equation (Fig. 3G) and is smaller than that of an equivalent 2D localized mode by roughly two orders of magnitude.

In accordance with Eq. 3, we also observed a marked increase in the Q of localized modes. To

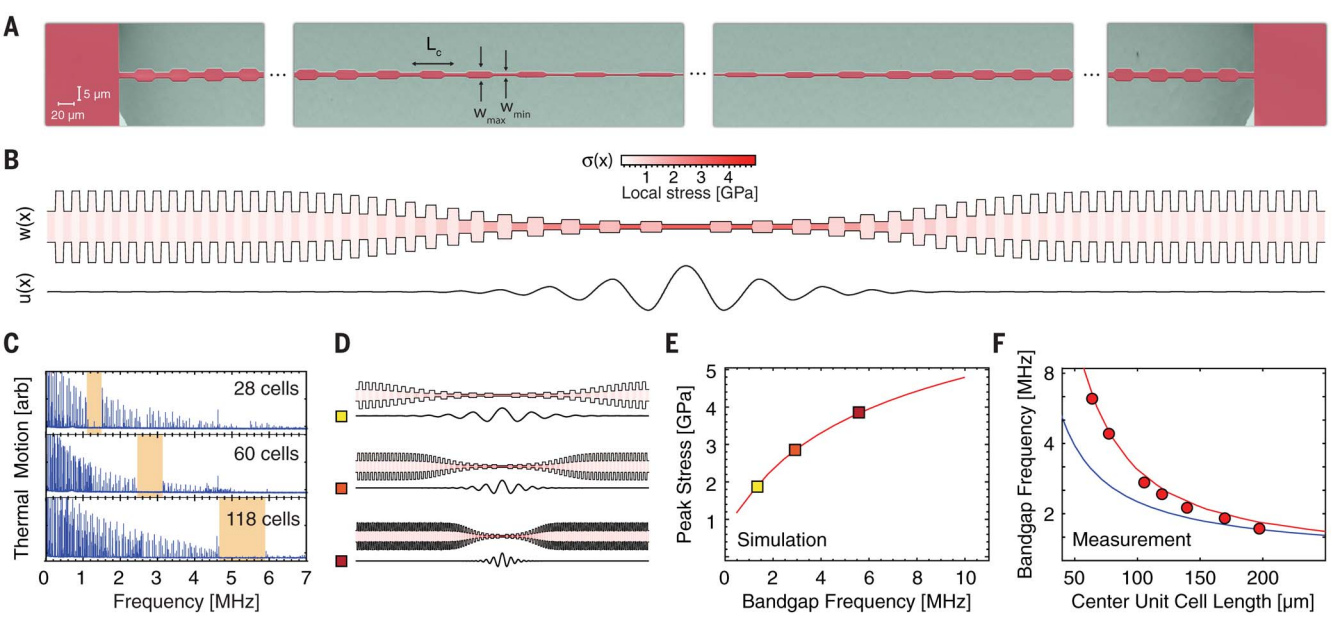

Fig. 2. Strain-engineered 1D phononic crystals. (**A**) Scanning electron microscopy (SEM) image of a tapered PnC nanobeam, vertically scaled for perspective. (**B**) Width/stress profile and defect mode shape of a device with 60 unit cells. (**C**) Thermal displacement spectrum of 4-mm-long devices. Band gaps are highlighted in orange. (**D**) Width/stress profiles of the devices in (C). (**E**) Simulation of peak stress versus band gap frequency f_{bg} for the devices shown in (D). (**F**) Measurements of f_{bg} versus length of the central unit cell (parameterizing the taper length). Red and blue lines are models with and without accounting for stress localization, respectively (see text).

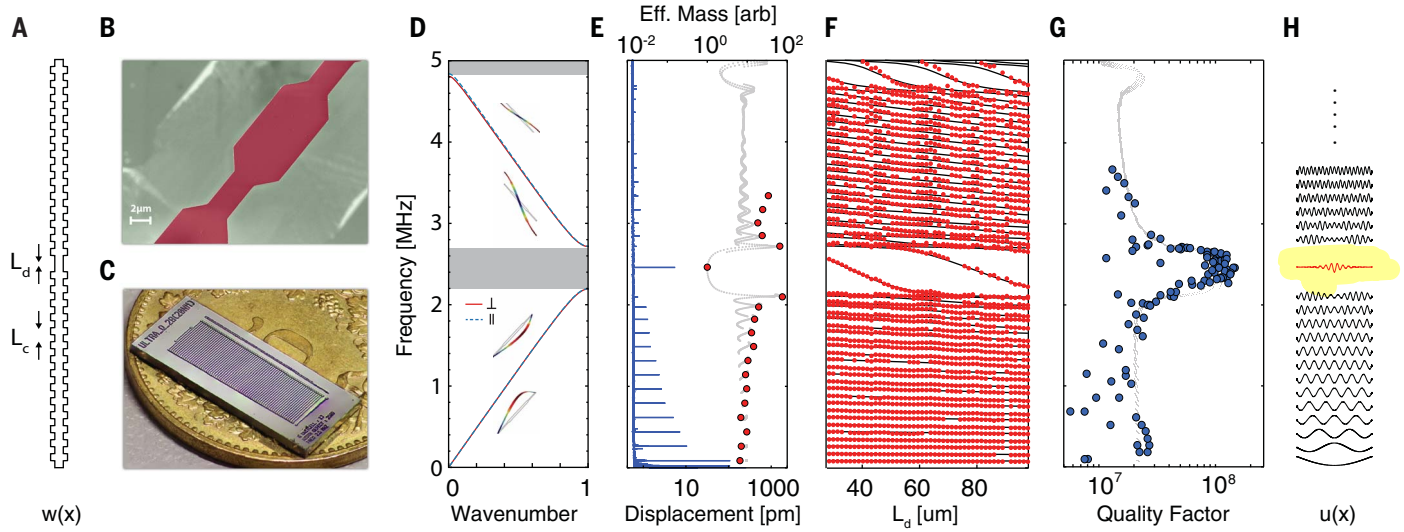

Fig. 3. "Soft-clamped" 1D nanomechanical resonators. (**A**) Schematic of a phononic crystal nanobeam with central defect. See text for details. (**B**) SEM image of a unit cell. (**C**) Optical image of a sample chip with 76 beams, each with a different defect length. (**D**) Band diagram showing in-plane (||) and out-of-plane (⊥) normal modes of a unit cell. (**E**) Displacement spectrum (blue) of a single beam, scaled to the theoretical root mean square thermal displacement of the defect mode, $\sqrt{k_B T/m_d(2\pi f)^2} \approx 6$ pm. Overlaid are effective mass coefficients m/m_d (red circles) inferred from the area beneath noise peaks. The gray curve is a model based on mode shapes in (H), used to estimate $m_d \approx 5$ pm (*20*). (**F**) Frequency spectra of multiple beams with different defect lengths. Black lines are a solution to the Euler-Bernoulli equation. (**G**) Compilation of Q measurements for a subset of the modes in (F), overlaid with a model based on Eq. 1. (**H**) Mode shapes obtained from the Euler-Bernoulli equation.

visualize this enhancement, we compiled measurements of Q versus mode frequency for 40 beams of different defect length (Fig. 3G). Outside the band gap, we find that $Q(f)$ is consistent with that of a uniform beam, asymptoting at low mode order (n < ~20) to $Q \approx 2 \times 10^7$, implying $Q_0 \approx 2\lambda Q \approx 1500$. Inside the band gap ($n \approx 26$), Q approaches that of an idealized clamp-free beam [$Q \approx Q_0/(\pi n \lambda)^2 \approx 10^8$]. The transition between these two regimes agrees well with a full model (gray dots in Fig. 3G) based on Eq. 1. In Fig. 4A we highlight the 19-s ringdown of a 2.46-MHz defect mode, corresponding to $Q = 1.5 \times 10^8$ and $Q \times f = 3.7 \times 10^{14}$ Hz.

Having established near-ideal soft-clamping of uniform nanobeams, we next studied the performance of strain-engineered (tapered) nanobeams. A set of 4- and 7-mm-long tapered PnC nanobeams was fabricated with the length of the taper varied so as to tune the stress at the center of the beam $\sigma(x_c)$ from 2 to 4 GPa (Fig. 2, D and E). We note that for our tapering strategy, the width of the beam center $w(x_c)$ is fixed, so that the stress is tuned by changing the equilibrium tension $\mathcal{T}$ (*20*). Moreover, for each taper length the soft-clamped mode is engineered to be well localized inside the thin taper region by tuning the pitch of unit cells. Measurements of band gap frequency f_{bg} versus length of the central unit cell length $L_{c,0}$ (parameterizing the taper length) corroborate enhanced stress through correspondence with the theoretical scaling $f_{bg} \propto \sqrt{\sigma(x_c)}/L_{c,0}$ (Fig. 2E).

The Q factors of uniform and tapered PnC nanobeams are compared in Fig. 4. Blue circles correspond to the measurements in Fig. 3G; red circles are compiled for localized modes of 4-mm-long tapered beams with various peak stresses, corresponding to f_{bg} = 1 to 6 MHz. According to a full model (*20*), $Q(f_{bg})$ should in principle trace out a line of constant $Q \times f \approx 10^{15}$ Hz, exceeding the clamp-free limit of a uniform beam ($Q \times f \propto 1/f$) for sufficiently high frequency. We observe this behavior with an unexplained ~30% reduction, with Q factors exceeding the clamp-free model by a factor of up to 3 and reaching absolute values high as 3×10^8. Although theoretically this Q should be accessible by soft-clamping alone at lower frequency, our strain-engineering strategy gives access to higher $Q \times f$, reaching a value as high as 8.1×10^{14} Hz for the 3.2-MHz mode of a 4-mm-long device. Higher Q and $Q \times f$ factors were achieved using longer beams (red squares in Fig. 4C). In Fig. 4A we highlight the 190-s ringdown of a 7-mm-long device excited in its 1.33-MHz defect mode, corresponding to $Q = 8.0 \times 10^8$ and $Q \times f = 1.1 \times 10^{15}$ Hz. We note that at this low damping rate ($f/Q \sim 1$ mHz), photothermal effects become important. Stroboscopic ringdowns (Fig. 4, A and B) confirm that photothermal damping contributes less than 5% uncertainty (*20*).

Realization of $Q \times f \sim 10^{15}$ in a mechanical oscillator with m on the order of picograms has numerous intriguing implications. First, such an oscillator is an exquisite force sensor. For example, localized modes of the beam outlined in Fig. 3 are limited by thermal noise to a sensitivity of $\sqrt{8\pi k_B T m f/Q} \approx 3(\mathrm{aN}/\sqrt{\mathrm{Hz}})$ at $f \sim 2.5$ MHz and $T = 300$ K. This value is on par with a typical atomic force microscope cantilever operating at a frequency and absolute temperature two orders of magnitude lower (*22*), creating new opportunities for applications such as high-speed force microscopy (*23*). Of practical importance is that the reported devices also exhibit an exceptionally strong thermal displacement of $\sqrt{k_B T Q/(4\pi^3 m f^3)} \sim \mathrm{nm}/\sqrt{\mathrm{Hz}}$, accessible by rudimentary detection techniques such as deflectometry. Indeed, their zero-point motion $\sqrt{\hbar Q/(2\pi^2 m f^2)} \sim \mathrm{pm}/\sqrt{\mathrm{Hz}}$ is orders of magnitude larger than the sensitivity of modern microcavity-based optical interferometers (*24*), offering possibilities in the field of quantum measurement and control (*25*). A fascinating prospect is to use measurement-based feedback to cool such an oscillator to its ground state from room temperature (*26*). A basic requirement is that the oscillator undergo a single oscillation in the thermal decoherence time $\hbar Q/k_B T$. The devices reported are exceptional in this respect, capable of performing $(2\pi Q \times f)/(k_B T/\hbar) > 100$ coherent oscillations at room temperature.

Looking forward, the performance of our devices seems far from exhausted. First, the dilution factors we have achieved are still an order of magnitude below the limit set by the yield stress of Si_3N_4. Our results may thus benefit from more aggressive strain engineering. [For example, Si microbridges have been fabricated with local stresses as high as 7.6 GPa (*14*).] We also emphasize that higher aspect ratios offer a direct route to higher Q. The aspect ratios of our longest beams ($L/h = 3.5 \times 10^5$) appear to be anomalously high for a suspended thin film, including 2D materials (*27*); however, Si_3N_4 membranes with centimeter-scale dimensions have recently been reported (*28*), hinting at a trend toward more extreme devices. Finally, we note that the source of intrinsic loss in our devices is unknown, although it is likely due to

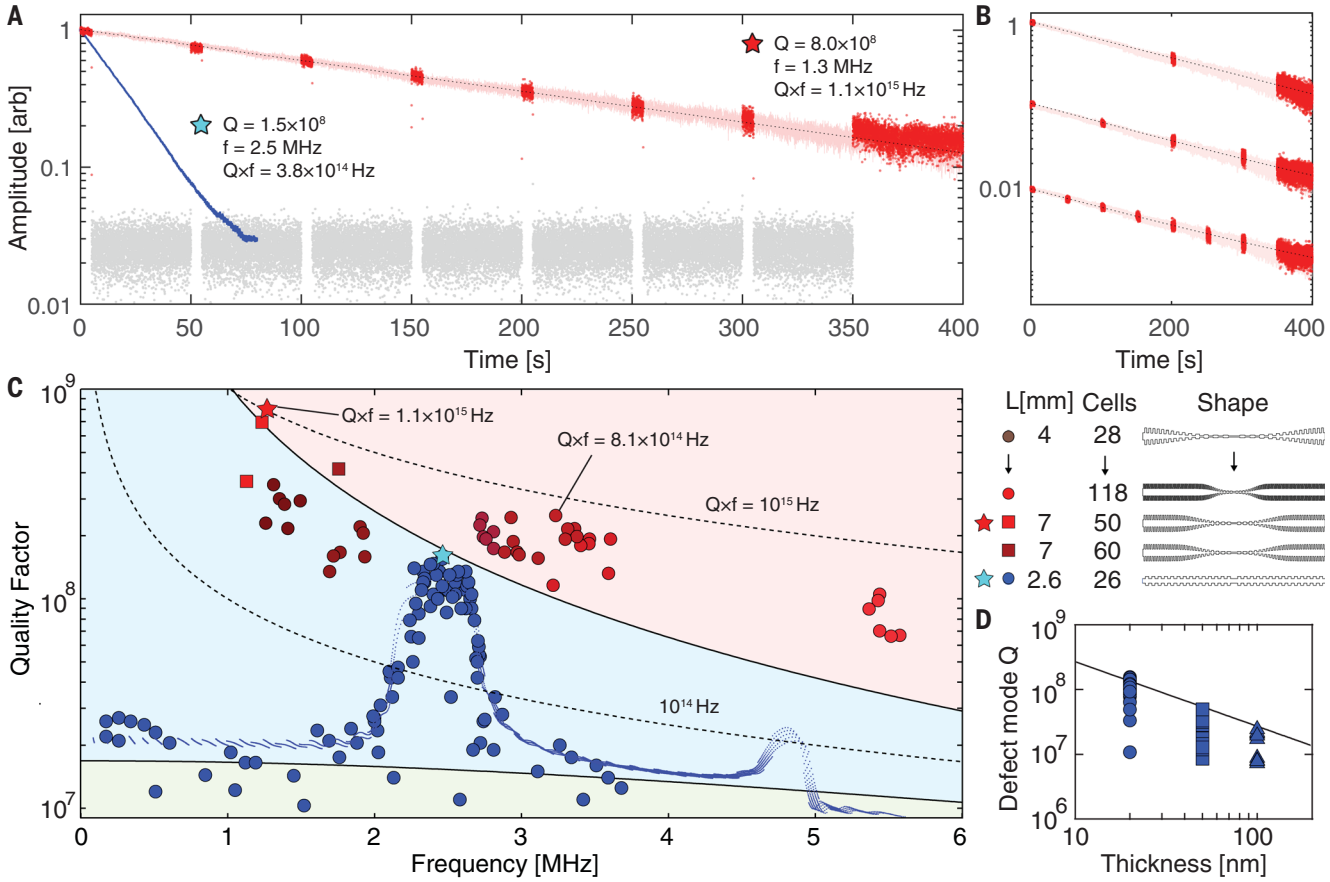

Fig. 4. Enhancing the quality factor of a soft-clamped nanobeam by strain engineering. (**A**) Interferometric ringdown of a 7-mm-long, 20-nm-thick tapered PnC nanobeam excited in its 1.33-MHz defect mode (pink). Dotted line is an exponential fit with a decay time of 190 s. The inferred Q of 8.0×10^8 is indicated by a red star in (C). Overlaid is a stroboscopic ringdown with measurement-on and measurement-off intervals in red and gray, respectively. (**B**) Fits to stroboscopic ringdowns with different duty cycles yield the same Q to within 5%, suggesting that photothermal damping is negligible. Also shown in (A) is a ringdown of a uniform PnC nanobeam [cyan star in (C)]. (**C**) Q versus mode frequency of PnC nanobeams with different geometries. Blue points correspond to modes of the uniform PnC nanobeam described in Fig. 3. Red points correspond to defect modes of tapered beams. Color groups include the highest five Q factors recorded for different beams. Blue dots are a numerical model based on Eq. 1. (**D**) Compilation of defect mode Q for uniform PnC nanobeams (Fig. 3) of different thickness. Overlaid is a model with $Q_0 = 6900 \cdot h/(100\ \text{nm})$, consistent with surface loss.

surface imperfections (*17*). To test this hypothesis, we compiled defect Qs for beams with thicknesses h = 20, 50, and 100 nm (Fig. 4D). The inferred thickness dependence of the intrinsic Q, $Q_0 \approx 6900 \cdot h/100$ nm, is indeed a signature of surface loss and agrees well in absolute terms with a recent meta-study on Si_3N_4 nanomechanical resonators (*17*). Remarkably, the $Q \propto Q_0/h^2$ scaling of soft-clamped resonators (*8*) preserves the advantage of thinner devices even in the presence of surface loss. It therefore seems appealing to apply our approach to epitaxially strained crystalline thin films (*29*), which can have Q_0 values two orders of magnitude larger than amorphous films at temperatures below 10 K (*30*).

REFERENCES AND NOTES

1. J. Li, Z. Shan, E. Ma, *MRS Bull.* **39**, 108–114 (2014).
2. J. Feng, X. Qian, C.-W. Huang, J. Li, *Nat. Photonics* **6**, 866–872 (2012).
3. P. Chidambaram, C. Bowen, S. Chakravarthi, C. Machala, R. Wise, *IEEE Trans. Electron Dev.* **53**, 944–964 (2006).
4. V. B. Braginsky, *Systems with Small Dissipation* (Univ. of Chicago Press, 1985).
5. G. I. González, P. R. Saulson, *J. Acoust. Soc. Am.* **96**, 207–212 (1994).
6. Q. P. Unterreithmeier, T. Faust, J. P. Kotthaus, *Phys. Rev. Lett.* **105**, 027205 (2010).
7. S. Schmid, K. D. Jensen, K. H. Nielsen, A. Boisen, *Phys. Rev. B* **84**, 165307 (2011).
8. Y. Tsaturyan, A. Barg, E. S. Polzik, A. Schliesser, *Nat. Nanotechnol.* **12**, 776–783 (2017).
9. D. R. Southworth *et al.*, *Phys. Rev. Lett.* **102**, 225503 (2009).
10. D. J. Wilson, C. A. Regal, S. B. Papp, H. J. Kimble, *Phys. Rev. Lett.* **103**, 207204 (2009).
11. S. Chakram, Y. S. Patil, L. Chang, M. Vengalattore, *Phys. Rev. Lett.* **112**, 127201 (2014).
12. D. Yu, J. Feng, J. Hone, *MRS Bull.* **39**, 157–162 (2014).
13. M. Süess *et al.*, *Nat. Photonics* **7**, 466–472 (2013).
14. R. A. Minamisawa *et al.*, *Nat. Commun.* **3**, 1096 (2012).
15. A. Castellanos-Gomez *et al.*, *Nano Lett.* **13**, 5361–5366 (2013).
16. P.-L. Yu, T. P. Purdy, C. A. Regal, *Phys. Rev. Lett.* **108**, 083603 (2012).
17. L. G. Villanueva, S. Schmid, *Phys. Rev. Lett.* **113**, 227201 (2014).
18. A. H. Ghadimi, D. J. Wilson, T. J. Kippenberg, *Nano Lett.* **17**, 3501–3505 (2017).
19. R. Zhang *et al.*, *Appl. Phys. Lett.* **107**, 131110 (2015).
20. See supplementary materials.
21. J. Chan, A. H. Safavi-Naeini, J. T. Hill, S. Meenehan, O. Painter, *Appl. Phys. Lett.* **101**, 081115 (2012).
22. M. Poggio, C. L. Degen, H. J. Mamin, D. Rugar, *Phys. Rev. Lett.* **99**, 017201 (2007).
23. M. Poggio, C. L. Degen, *Nanotechnology* **21**, 342001 (2010).
24. M. Aspelmeyer, T. J. Kippenberg, F. Marquardt, *Rev. Mod. Phys.* **86**, 1391–1452 (2014).
25. D. J. Wilson *et al.*, *Nature* **524**, 325–329 (2015).
26. Y.-C. Liu *et al.*, *Phys. Rev. A* **91**, 013824 (2015).
27. R. A. Barton *et al.*, *Nano Lett.* **11**, 1232–1236 (2011).
28. J. P. Moura, R. A. Norte, J. Guo, C. Schäfermeier, S. Gröblacher, arXiv:1707.08128 [physics.optics] (25 July 2017).
29. G. D. Cole *et al.*, *Appl. Phys. Lett.* **104**, 201908 (2014).
30. G. D. Cole, W. Zhang, M. J. Martin, J. Ye, M. Aspelmeyer, *Nat. Photonics* **7**, 644–650 (2013).

ACKNOWLEDGMENTS

We thank H. Schütz and E. Mansouri for valuable contributions during the initial phase of the experiment. **Funding:** Supported by the EU Horizon 2020 Research and Innovation Program under grant agreement 732894 (FET Proactive HOT) and the SNF Cavity Quantum Optomechanics project (grant 163387); MSCA ETN-OMT grant 722923 (M.J.B.); ERC AdG QuREM grant 320966 (T.J.K.); and DARPA seedling grant HR0011181003. All samples

were fabricated at the Center for MicroNanoTechnology (CMi) at EPFL. **Author contributions:** Device design and simulation was led by A.H.G. and S.A.F. with early support from R.S.; devices were fabricated by A.H.G. and M.J.B.; S.A.F. developed the semi-analytical model; all authors contributed to measurements and/or development of the experimental apparatus; data analysis was led by N.J.E., S.A.F., and D.J.W. with support from A.H.G. and M.J.B.; the manuscript was initially drafted by D.J.W. and S.A.F. with support from N.J.E.; D.J.W., S.A.F., N.J.E., A.H.G., M.J.B., and T.J.K. all participated in editing of the final manuscript and supporting information; and D.J.W. and T.J.K. supervised the project. **Competing interests:** None declared. **Data and materials availability:** Data and data analysis code are available through Zonedo at doi:10.5281/zenodo.1202322. All other data needed to evaluate the conclusions in the paper are present in the paper or the supplementary materials.

SUPPLEMENTARY MATERIALS

www.sciencemag.org/content/360/6390/764/suppl/DC1
Supplementary Text
Figs. S1 to S12

8 December 2017; accepted 28 March 2018
Published online 12 April 2018
10.1126/science.aar6939